Designing Glass and Crystalline Phases of Metal−Bis(acetamide) Networks to Promote High Optical Contrast

Mengtan Liu, Adam H. Slavney, Songsheng Tao, Ryan D. McGillicuddy, Cassia C. Lee, Malia B. Wenny, Simon J. L. Billinge, and Jarad A. Mason*

Read Online

ACCESS | Metrics & More | Article Recommendations | Supporting Information

ABSTRACT: Owing to their high tunability and predictable structures, metal−organic materials offer a powerful platform to study glass formation and crystallization processes and to design glasses with unique properties. Here, we report a novel series of glass-forming metal−ethylenebis(acetamide) networks that undergo reversible glass and crystallization transitions below 200 °C. The glass-transition temperatures, crystallization kinetics, and glass stability of these materials are readily tunable, either by synthetic modification or by liquid-phase blending, to form binary glasses. Pair distribution function (PDF) analysis reveals extended structural correlations in both single and binary metal−bis-(acetamide) glasses and highlights the important role of metal−

metal correlations during structural evolution across glass−crystal transitions. Notably, the glass and crystalline phases of a Co−ethylenebis(acetamide) binary network feature a large reflectivity contrast ratio of 4.8 that results from changes in the local coordination environment around Co centers. These results provide new insights into glass−crystal transitions in metal−organic materials and have exciting implications for optical switching, rewritable data storage, and functional glass ceramics.
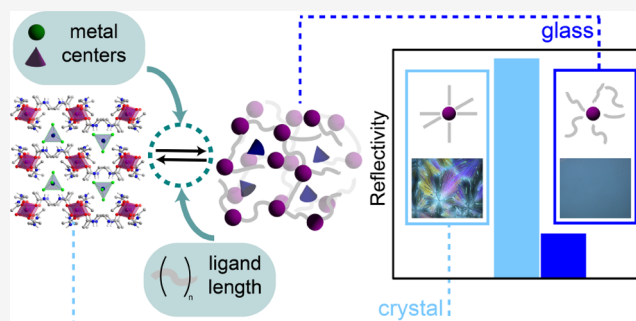
INTRODUCTION

With the structural disorder characteristic of a liquid and the restricted dynamics characteristic of a solid, glasses are optically transparent, highly processable, and grain-boundary-free materials that play an important role in many current and emerging technologies.[1−3] Glasses are critical components of displays,[4] coatings,[5] and building materials,[6] and new glassy materials are being actively developed as solid electrolytes for batteries,[7] storage media for radioactive waste,[8] and matrices to isolate qubits for quantum computing.[9] Though many inorganic, metallic, polymeric, and molecular organic materials can form glasses,[2,10] the compositional and structural diversity of glasses that have been designed, synthesized, and studied to date pales in comparison to crystalline materials. For instance, extended metal−organic materials offer tremendous potential for dramatically expanding the library of materials with accessible glass phases yet have only recently begun to receive attention in this context. Owing to their high tunability and the predictable, directional nature of interactions between metal cations and bridging organic ligands,[11] glasses formed from extended networks of coordination bonds can enable the establishment of more robust structure−property relationships than are typically possible for conventional glasses and provide access to new functionalities that arise from unique mechanical, electronic, optical, and host−guest properties not found in traditional inorganic or organic glasses.

Glassy materials are distinguished from amorphous powders by their ability to undergo a thermally induced transition—the glass transition—from a rigid solid to a dynamic liquid that can be molded into transparent objects of arbitrary size and shape with isotropic properties.[2,12] Although there are many examples of amorphous metal−organic materials,[13] the range of metal−organic glasses is far more limited.[14] To date, glass transitions have been realized for only a small subset of extended metal−organic materials, including, most prominently, zeolitic−imidazolate frameworks (ZIFs),[15] zinc−phosphate and metal−thiocyanate coordination polymers,[16] and two- and three-dimensional perovskites.[17] The diversity of metal−organic glasses is limited, in part, by the high melting temperatures—often near or above ligand decomposition temperatures—of most extended metal−organic materials,[15b,16b] which precludes glass formation via melt quenching. Melt quenching is one of the most powerful and versatile methods for glass formation because the structure and properties of glass can be controlled by the specific

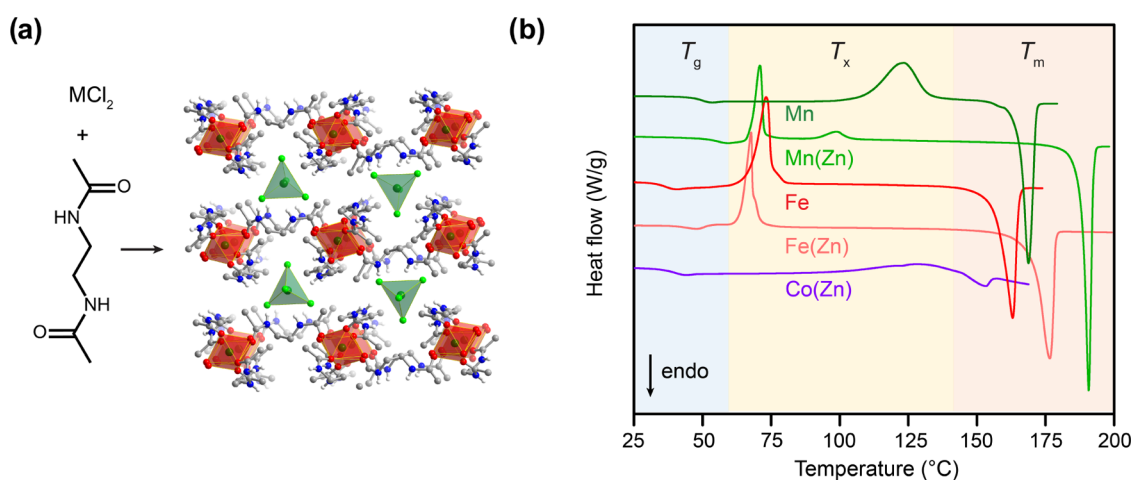**Figure 1.** (a) Crystal structure of two-dimensional framework $Mn(eba)_3[MnCl_4]$ at 298 K. Note that at 298 K, one of the two crystallopgrahically independent eba ligands is disordered over two symmetry-related positions, and only one of them is shown for simplicity. Olive, red, gray, blue, green, and white spheres represent Mn, O, C, N, Cl, and H atoms, respectively; only N−H protons are shown. The range of transition temperatures (T_g, T_x, T_m) is highlighted with light blue, yellow, and orange, respectively. (b) DSC traces for $M(eba)_3[M'Cl_4]$ (M/M′ = Fe, Mn; and M = Co, Fe, Mn, M′ = Zn) with a heating rate of 5 °C/min for all compounds. The DSC traces are offset by 0.5 W/g from each other for clarity. The range of temperatures that correspond to glass transitions (T_g), cold crystallizations (T_x), and melting transitions (T_m) are highlighted in light blue, yellow, and orange, respectively.

nonequilibrium conditions used to cool a melt from an equilibrium liquid phase to a supercooled liquid and, ultimately, metastable solid glass.[2b,c,18]

Recently, we reported a series of two- and three-dimensional metal−bis(acetamide) networks that feature record-low melting temperatures and form stable liquid phases that can, in many cases, be quenched into a glass phase.[19] In some of these materials, the crystal-to-glass transition is reversible, and both a glassy and crystalline solid can be accessed from the liquid state, depending on the exact thermal profile followed after a melting or glass transition. This is rare for metal−organic glasses, as crystalline phases are not typically accessible under any thermal cycling conditions. To the best of our knowledge, thermally induced reversible glass−crystal transitions have not been observed for any other classes of three-dimensional metal−organic frameworks and have only been realized for a hybrid perovskite, as well as a few one- and two-dimensional metal−organic coordination polymers.[16a,17b]

The predictable and reversible conversion between crystal and glass phases offers opportunities for fabricating thin films and glass ceramics with precisely tailored properties.[20,21] Moreover, reversible glass−crystal transitions underpin technologies such as nonvolatile data storage and memory, optical switching, and reflective displays, which rely on materials that can be switched between states with large differences in electrical resistivity or optical reflectivity.[22,23] Chalcogenides have received the most attention as electronic and optical phase-change materials because of the high contrast in conductivity and reflectivity between their glass and crystalline phases and their ability to be rapidly interconverted.[23c] However, the high melting temperatures of chalcogenides (~500 to 800 °C) lead to much greater energy requirements for thermal switching in comparison to that for a typical transistor.[24,25] Meltable metal−organic materials provide an opportunity to reduce this thermal budget by achieving high electronic and optical contrast between a glassy and crystalline phase at much lower transition temperatures.[26] Indeed, a reversible glass−crystal transition accompanied by a distinct shift in the optical absorption onset was recently demonstrated

for a hybrid layered perovskite with a low melting temperature of 175 °C.[17b] Much remains to be understood, however, about how to systematically design metal−organic materials that undergo glass−crystal transitions at low temperatures with fast kinetics, high reversibility, and changes in properties tailored for specific applications.

Given that metal−bis(acetamide) networks experience a decrease in average metal coordination number upon melting,[19] it should be possible to design networks composed of optically active transition metals with high optical contrast between crystalline and glass phases. In particular, we anticipated that $d−d$ electronic transitions that are Laporte-forbidden for centrosymmetric octahedral metal centers in the crystalline network would become allowed for lower-coordinate metal centers in the glassy phase. The glass-transition temperatures of our previously reported metal−butylenebis(acetamide) networks, however, are near or below ambient temperature,[19] which makes it challenging to rigorously characterize their properties and is impractical for most applications. Herein, we report a new series of glass-forming two-dimensional metal−ethylenebis(acetamide) networks that undergo glass transitions above ambient temperature. Through liquid-phase blending and judicious selection of different components of the network, we show that reversible switching between glass and crystalline phases with large differences in optical reflectivity can be achieved, revealing a promising pathway for optical switching in metal−organic glasses.

■ RESULTS AND DISCUSSION

Glass Formation and Recrystallization Behavior. To design metal−bis(acetamide) networks with higher glass-transition temperatures than glasses composed of hexamethylenebis(acetamide) (hmba, n = 6) and butylenebis-(acetamide) (bba, n = 4) bridging organic ligands, the shorter ligand N,N′-ethylenebis(acetamide) (eba, n = 2) was combined with divalent transition-metal chloride salts to yield a new series of two-dimensional $M(eba)_3[M'Cl_4]$ networks (M = M′ = Mn, Fe and M = Mn, Fe, Co for M′ =

Zn). Single-crystal X-ray diffraction (SCXRD) revealed that all compounds crystallize in the same orthorhombic space group (*Pbcm*) with the same extended connectivity, wherein two pairs of ligands connect each octahedral metal center to two different neighboring metal centers to form one-dimensional chains. An additional pair of ligands bind two metal centers orthogonal to the chains, interconnecting them to afford two-dimensional sheets of coordination networks that are stacked around layers of charge-balancing tetrahedral $[M'Cl_4]^{2-}$ anions (Figure 1a). Except for $Co(eba)_3[ZnCl_4]$, which undergoes a partial recrystallization, all $M(eba)_3[M'Cl_4]$ networks undergo a fully reversible melting transition (T_m) between 150 and 190 °C and form glasses upon fast quenching (20−50 °C/min) with glass-transition temperatures (T_g) that range from 33 °C for $Fe(eba)_3[FeCl_4]$ to 50 °C for $Mn(eba)_3[ZnCl_4]$. Moreover, cold crystallization transitions (T_x), which correspond to an amorphous-to-crystalline transition induced by heating below T_m, are observed for each network by differential scanning calorimetry (DSC) and powder X-ray diffraction (PXRD) on subsequent heating runs after glass formation (Figures 1b and S6).

Comparing glass-transition temperature for the $M(eba)_3[M'Cl_4]$ networks to those of glass-forming hmba- and bba-containing networks reveals an inverse correlation between the length of the polymethylene chain, n, and T_g (Figure 2, top). Though moderate on an absolute scale, there is also an inverse correlation between n and T_m (Figure 2, middle). The increase in T_m is primarily driven by a decrease in the entropy of fusion, ΔS_{fus} (Figure 2, bottom), which can be attributed to the lower conformational flexibility of the shorter
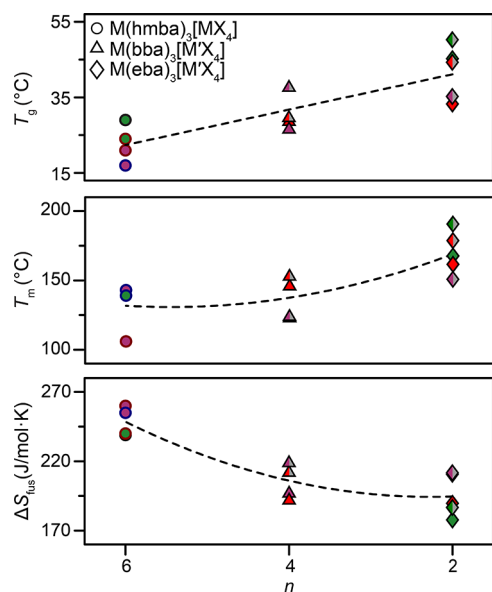
polymethylene bridge reducing the difference in rotational and configurational entropy between the solid and liquid states.[27] The shorter polymethylene chain likely also contributes to a higher T_g by increasing the viscosity of the molten phase (Figure S43), which leads to slower relaxation dynamics and promotes glass formation at higher temperatures.

Interestingly, the identity of the metal center in the metal tetrahalide counteranion (M′) has a substantial effect on the melting transitions of $M(eba)_3[M'Cl_4]$, which contrasts with the $M(bba)_3[M'Cl_4]$ compounds wherein the identity of the counteranion minimally affects T_m. For instance, $Fe(eba)_3[FeCl_4]$ and $Mn(eba)_3[MnCl_4]$ have melting temperatures of 162 and 167 °C, respectively, and replacing the counteranion with $[ZnCl_4]^{2-}$ leads to increases in T_m to 178 and 189 °C, respectively. The increase in T_m is primarily driven by an increase in the enthalpy of fusion, ΔH_{fus}, that is not compensated for by a commensurate increase in ΔS_{fus} (Figure S11). This can be rationalized, in part, through variable-temperature SXCRD, which reveals dynamic disorder in the $M(eba)_3[M'Cl_4]$ networks (Figure S4) that is absent in $M(bba)_3[M'Cl_4]$ and suggests a greater residual entropy in the solid state of the former compounds. Since the $[M'Cl_4]^{2-}$ anions are engaged in hydrogen-bonding interactions with the N−H protons of the eba ligand, stronger hydrogen bonds to the more electron-rich Cl atoms of $[ZnCl_4]^{2-}$ anions should lead to a larger ΔH_{fus} than the more electron-poor Cl atoms of $[FeCl_4]^{2-}$ and $[MnCl_4]^{2-}$. Because each $[M'Cl_4]^{2-}$ anion only engages in hydrogen-bonding interactions with one metal−organic layer (Figure S2), we hypothesize that hydrogen-bonding strength has less of an effect on restricting the residual motion—and lowering the entropy—of $[M'Cl_4]^{2-}$ anions and bis(acetamide) ligands in the solid state for the two-dimensional $M(eba)_3[M'Cl_4]$ networks than for the three-dimensional $M(bba)_3[M'Cl_4]$ networks for which $[M'Cl_4]^{2-}$ anions are engaged in hydrogen bonds to the surrounding metal−organic network in all three dimensions (Figure S2). This would explain why there is greater enthalpy−entropy compensation in the latter case than in the former and is consistent with the increased dynamic disorder revealed by variable-temperature SXCRD for the $M(eba)_3[M'Cl_4]$ network compared to $M(bba)_3[M'Cl_4]$ (Figure S4).

In addition to its impact on melting thermodynamics, the introduction of $[ZnCl_4]^{2-}$ also has a marked influence on the crystallization kinetics and glass-forming ability of each compound. For example, $Mn(eba)_3[ZnCl_4]$ requires a cooling rate of at least 50 °C/min to circumvent crystallization and form a glass during DSC experiments, while $Mn(eba)_3[MnCl_4]$ forms a glass for cooling rates faster than 30 °C/min. On subsequent heating, T_x of $Mn(bba)_3[MnCl_4]$ is also 36 °C higher than that of $Mn(bba)_3[ZnCl_4]$. These differences are further reflected in the higher glass stability of $Mn(eba)_3[MnCl_4]$, which describes how resistant glass is to devitrification upon heating and is critical to evaluating reversible glass−crystal transitions.[28] There are several empirical parameters that can be used to quantify glass stability, including the Hrubý parameter (K_H),[29] which is related to normalized differences between T_x and T_g and is calculated as:

Figure 2. Trends in T_g (top), T_m (middle), and ΔS_{fus} (bottom) are illustrated for glass-forming metal−bis(acetamide) networks with various bridging polymethylene chain lengths, n. Black dotted lines represent a linear fit of the average T_g as a function of n ($r^2 = 0.66$) and polynomial fits of the average T_m ($r^2 = 0.51$) and ΔS_{fus} ($r^2 = 0.76$) as a function of n. The color of the symbol denotes the nature of the metal centers. Solid green, red, and purple represent M = M′ = Mn, Fe, Co, respectively, while a combination of colors represents compounds with M′ = Zn. The color of the outline of the symbol denotes the nature of halides on the counteranion site, with black, brown, and dark blue representing Cl, Br, and NCS, respectively.

$$K_H = \frac{(T_x - T_g)}{(T_m - T_x)} \qquad (1)$$

With a K_H of 0.13, $Mn(eba)_3[ZnCl_4]$ is classified as an unstable glass that should be challenging to isolate experimentally. Consistent with its higher glass-forming ability, the K_H of $Mn(eba)_3[MnCl_4]$ increases by almost 7-fold to 0.88, which is within the empirical K_H range of 0.5−1.0 that typically permits facile glass preparation. Even though the difference is smaller, the glass stability of $Fe(eba)_3[FeCl_4]$ (K_H = 0.37) is also higher than $Fe(eba)_3[ZnCl_4]$ (K_H = 0.22), which suggests that $[ZnCl_4]^{2-}$ consistently leads to a decrease in glass stability.

In addition to glass stability, we also directly probed differences in the kinetics of recrystallization between $Mn(eba)_3[MnCl_4]$ and $Mn(eba)_3[ZnCl_4]$. Specifically, we used DSC experiments to measure the time required for complete isothermal cold crystallization of each compound as a function of temperature in the vicinity of their respective T_x (Figure S16). For both compounds, the fraction of crystallization, α, as a function of time at each temperature can be well modeled (r^2 > 0.99) by the Avrami equation[30]

$$\alpha(t) = 1 - \exp(-k^n(t - t_0)^n) \tag{2}$$

where k is the crystallization rate constant, n is the Avrami exponent that depends on the nucleation and growth mechanism, and t_0 is the induction time of crystallization (Figure S16). The higher k and n values modeled for $Mn(eba)_3[ZnCl_4]$ indicate faster recrystallization kinetics and are consistent with the lower glass-forming ability of this compound compared to $Mn(eba)_3[MnCl_4]$ (Table S10). The temperature dependence of k is related to the activation energy, E_a, for crystallization. The rate constants for $Mn(eba)_3[ZnCl_4]$ follow typical Arrhenius behavior and can be described by

$$k(T) = A \exp\left(\frac{-E_a}{RT}\right) \tag{3}$$

where A is the pre-exponential coefficient and R is the ideal gas constant, yielding an activation energy of 200 kJ/mol that is similar to values reported for the crystallization of some inorganic glasses.[31] Interestingly, the temperature dependence of k for $Mn(eba)_3[MnCl_4]$ appears to be non-Arrhenius and can be modeled by two processes with an activation energy of 56 kJ/mol at lower temperatures and an activation energy of 234 kJ/mol at higher temperatures (Figure 3). We note that larger sample-to-sample variation is observed at higher temperatures, which may indicate the presence of other processes not accounted for in the model. The lower E_a of $Mn(eba)_3[ZnCl_4]$ could be rationalized by stronger hydrogen-bonding interactions between $[M'Cl_4]^{2-}$ and the N−H proton in the eba ligand in the glass state relative to $Mn(eba)_3[MnCl_4]$, leading to less bond rearrangement during crystallization. This is corroborated by infrared (IR) spectroscopy, which reveals that the N−H stretch ($\sim$3290 cm^{-1}) of glassy $Mn(eba)_3[ZnCl_4]$ is less red-shifted (by $\sim$10 cm^{-1}) from its crystalline state in comparison to glassy $Mn(eba)_3[ZnCl_4]$ (Figure S44).

Formation of Binary Metal−bis(acetamide) Glasses. High glass stability is typically required for applications, such as phase-change memory and rewritable data storage, that leverage a contrast in optical properties between crystalline and glassy states of a material. All $M(eba)_3[M'Cl_4]$ compounds except for $Mn(eba)_3[MnCl_4]$ have relatively low glass stability (K_H < 0.5), but the spin-forbidden $d−d$ transitions of the high-
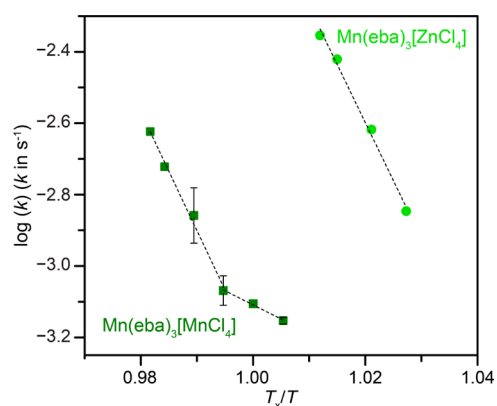

Figure 3. Temperature dependence of the crystallization rate constants for $Mn(eba)_3[MnCl_4]$ and $Mn(eba)_3[ZnCl_4]$ are shown as olive squares and light green circles, respectively. The measurement temperatures are normalized to the crystallization onset temperature, and black dotted lines represent Arrhenius fits (r^2 > 0.98). Representative error bars are shown for $Mn(eba)_3[MnCl_4]$ at 3 T_x/T values and reflect variations between 2 and 3 independently synthesized samples.

spin Mn(II) centers—and, consequently, the optical properties of the compound—are minimally affected by changes in coordination number. In an effort to increase the glass stability of networks containing more optically active metals, we discovered that multiple $M(eba)_3[ZnCl_4]$ networks could be combined to form new binary **1**-$M^1/M^2(Zn)$ phases with substantially higher glass stability. For example, mixing $Mn(eba)_3[ZnCl_4]$ and $Co(eba)_3[ZnCl_4]$ in a 1:1 ratio by mechanical grinding followed by melting and recrystallization resulted in the new homogeneous phase **1**-Mn/Co(Zn), which undergoes a single glass transition, cold crystallization, and reversible melting transition. Relative to the two parent networks, the new melting transition occurs at an intermediate temperature with a slightly lower ΔH_{fus}. The reversibility of the glass−crystal transition in this binary phase and the large ΔH_{fus} recovery are surprising, as less than 4% of the melting enthalpy could be recovered during partial recrystallization of the single-phase $Co(eba)_3[ZnCl_4]$ network. In addition, **1**-Mn/Co(Zn) features a much higher K_H of 0.79 than $Mn(eba)_3[ZnCl_4]$ (K_H = 0.13), demonstrating how glass stability can be readily tuned by mixing without adversely affecting reversibility.

Although liquid-phase blending of ZIFs typically leads to domain-structured glasses,[32] SEM-EDX reveals that Mn, Co, and Zn are distributed homogeneously throughout the **1**-Mn/Co(Zn) binary glass (Figure 4). Moreover, PXRD confirms that recrystallized **1**-$M^1/M^2(Zn)$ compounds are isostructural to the parent $M(eba)_3[ZnCl_4]$ networks (Figure S7). The SEM and PXRD analysis—along with DSC experiments that show single melting transitions for all consecutive heating runs of the mixed phase (Figure 4a)—suggest that the metal centers from the parent networks are evenly distributed throughout the coordination network, likely via the dynamic dissociation and association of metal−ligand bonds within the molten and supercooled liquid states that promote the formation of $M^1−$eba−M^2 linkages. As such, we expect liquid-phase mixing to be generalizable to a wide range of metal−bis(acetamide) networks, enabling the formation of mixed glasses with glass stability and crystallization behavior tailored for specific applications (Figure S15).
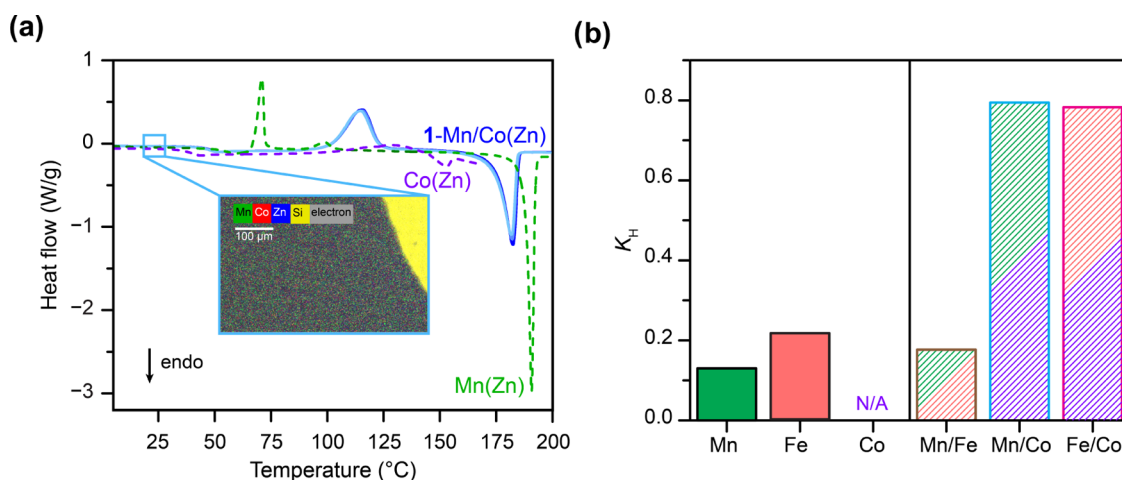
Figure 4. (a) DSC traces of $Co(eba)_3[ZnCl_4]$, $Mn(eba)_3[ZnCl_4]$ networks, and **1**-Mn/Co(Zn) with a heating rate of 5 °C/min for all compounds. Purple and green dotted lines correspond to the 2nd heating runs for $Co(eba)_3[ZnCl_4]$ and $Mn(eba)_3[ZnCl_4]$, respectively, and the blue solid lines correspond to the 2nd−4th heating runs of **1**-Mn/Co(Zn) (from dark to light). Inset: A SEM-EDS image of a **1**-Mn/Co(Zn) glass film showing the homogeneous distribution of Mn, Co, and Zn atoms through the entire glass. (b) Hrubý parameters (K_H) describing glass stability of $M(eba)_3[ZnCl_4]$ networks (left) and **1**-M^1/M^2(Zn) binary networks (right, (Zn) omitted from the labels for clarity) obtained from combining any two of the $M(eba)_3[ZnCl_4]$ networks show enhanced glass stability in binary networks. K_H of $Co(eba)_3[ZnCl_4]$ could not be determined because of incomplete crystallization.
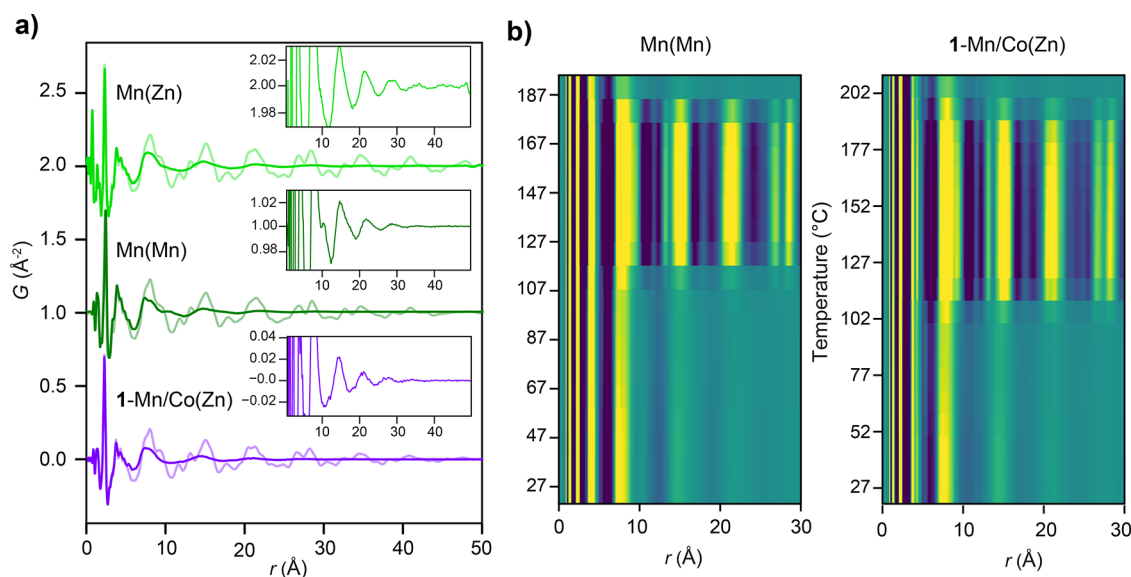

Figure 5. (a) Pair distribution function (PDF) of the ambient-temperature glass phase (dark traces) and high-temperature crystalline phase (light traces) of $Mn(eba)_3[ZnCl_4]$ (green), $Mn(eba)_3[MnCl_4]$ (olive), and **1**-Mn/Co(Zn) (purple). An oscillatory signal indicative of extended-range ordering for each glass is shown in the insets. (b) Variable-temperature PDFs of $Mn(eba)_3[MnCl_4]$ (left) and **1**-Mn/Co(Zn) (right) as the temperature is increased through a glass−crystal and then crystal−liquid transition.

In Situ Structural Analysis of Glass−Crystal Transitions. To further investigate glass−crystal transitions in both single and binary $M(eba)_3[M'Cl_4]$ compounds, we collected variable-temperature X-ray total scattering data for $Mn-(eba)_3[MnCl_4]$, $Mn(eba)_3[ZnCl_4]$, and **1**-Mn/Co(Zn). The raw total scattering data was integrated, corrected for experimental effects, and normalized using PDFgetX3 to obtain total scattering-reduced structure functions, $F(Q)$, which were Fourier transformed to get pair distribution functions (PDFs), $G(r)$ (Figure 5a).[33] Glassy samples showed broad diffuse scattering peaks and did not contain any of the strong features at high-r ($r > 20$ Å) in $G(r)$ that are characteristic of crystalline samples.

The PDFs of $M(eba)_3[M'Cl_4]$ networks provide insight into the structure of the disordered glassy states (Figure 5). At short interatomic distances ($0 < r < 5$ Å), the glass-phase PDFs are very similar to those of the crystalline phase, with sharp features that can be assigned to C−C, C−N, and C−O bonds within the eba ligands and to M−O and M'−Cl bonds, suggesting minimal changes to local coordination environments (Figure S24). This is consistent with ambient-temperature X-ray absorption fine structure (EXAFS) data for glassy $Mn(eba)_3[MnCl_4]$, which can be well modeled with half of the Mn centers coordinated to 4 Cl atoms—consistent with the $[MnCl_4]^{2-}$ anion being preserved in the glassy state—and half of the Mn centers coordinated to 4.4(1.2) O atoms of the eba ligand (Figure 6). The average metal−ligand coordination
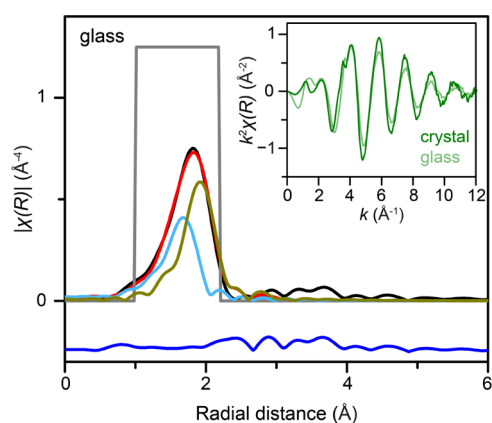
Figure 6. EXAFS model for glassy $Mn(eba)_3[MnCl_4]$. Black traces correspond to experimental data, while red, light blue, and dark yellow traces represent the overall Mn–O, and Mn–Cl fits, respectively, and residuals are shown in blue. The fitting window (gray) is from 1.0 to 2.2 Å. Inset: k space representations of the EXAFS data for crystalline (olive) and glassy (light green) $Mn(eba)_3[MnCl_4]$ showing minimal changes from the crystalline state upon glass formation.

number of 4.4(1.2) is comparable to that of the molten phase of $Co(bba)_3[CoCl_4]$ ($N_{Co-O} = 4.8(7)$) and is well above the

bond percolation threshold of 2.0–2.4 that is required for a disordered network.[19,34] This is consistent with the presence of an extended network of metal–ligand coordination interactions—rather than discrete molecular units—that spans the entire glass.

The intermediate-r ($5 < r < 20$ Å) and high-r ($r > 20$ Å) regions of the PDFs of $M(eba)_3[M'Cl_4]$ glasses further reveal structural ordering reminiscent of the parent crystalline phases. For instance, calculations of PDF patterns based on the crystalline phase show that peaks at 8.1 and 15 Å arise mostly from first- and second-nearest-neighbor correlations between framework and counteranion metal centers (M–M'), while peaks at 9.5 and 13 Å mainly arise from M–M and M–M' correlations. Though decreased in intensity in the glassy phases, broad peak features centered at 7.8 and 14.5 Å suggest structural correlations reminiscent of first- and second-nearest-neighbor metal–metal correlations in the crystalline state, albeit with a much wider distribution of metal–metal distances (Figure S31). In addition, a close examination of PDF patterns beyond 20 Å reveals an oscillatory signal that extends to 40 Å for all three $M(eba)_3[M'Cl_4]$ glasses (Figure 5a, inset). This oscillatory signal can be attributed to density modulations that persist in the glassy state and produce a relatively sharp feature at low-Q in the diffraction signal known as the first sharp
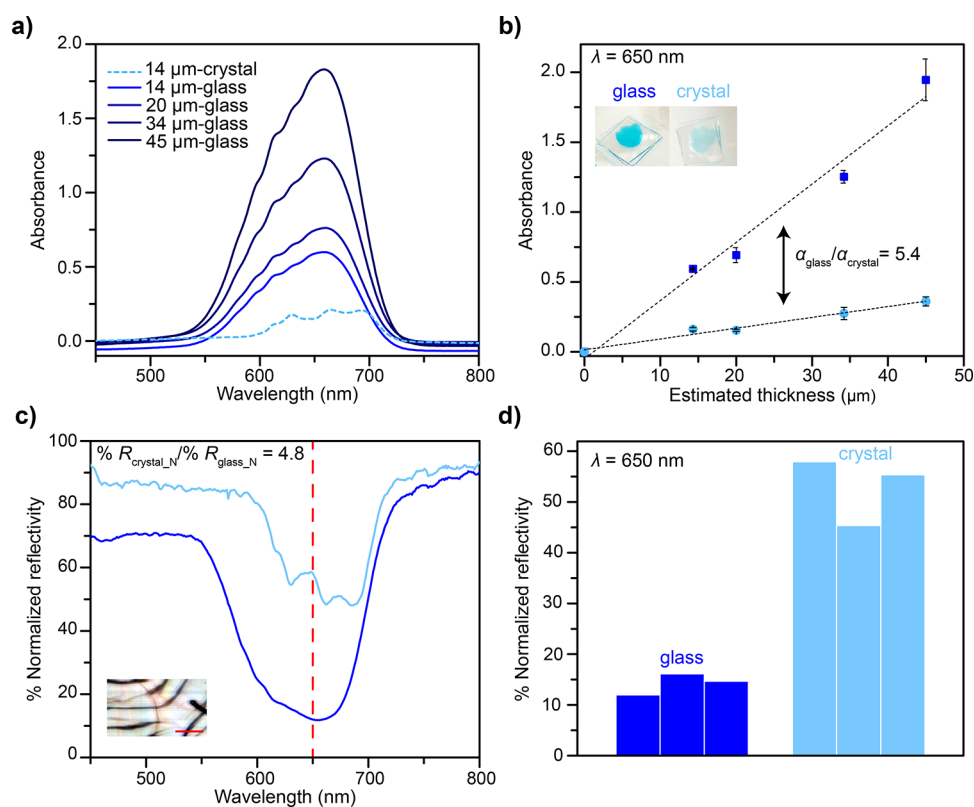

Figure 7. (a) UV–vis spectra of a crystalline **1**-Mn/Co(Zn) film (dotted line) compared to glassy films with a range of estimated thicknesses (solid lines). (b) Absorbances at 650 nm as a function of estimated thickness for glassy (dark blue squares) and crystalline (light blue circles) films. Black dotted lines represent Beer's law fits ($r^2 \geq 0.97$), and the slope of each fit corresponds to the absorption coefficient α. Inset: picture of a presentative **1**-Mn/Co(Zn) glass film (left) and the same film after annealing (right). (c) High reflectivity contrast ratio of 4.8 at 650 nm (red dotted line) across a melt quench-annealing cycle of a **1**-Mn/Co(Zn) film. The % normalized reflectivity of the glass and crystalline film is shown in dark and light blue solid lines, respectively. Inset: optical images of the measured crystalline film, from which a single grain, with size ~15 μm in width, was selected for data analysis. The scale bar corresponds to 10 μm. (d) Cycling experiment results demonstrating well-retained reflectivity contrast. A **1**-Mn/Co(Zn) film was cycled between the glass and the crystalline states seven times, and three reflectivity measurements were taken for each phase at different cycles. The variability between each measurement for crystalline and glassy films likely arises from slight changes in the film thickness after melting.

diffraction peak (FSDP).[35] The FSDP is a common feature of network-forming liquids and amorphous solids, and its position, Q_1, is correlated to the wavelength of the oscillatory signal, λ, as described by[36]

$$\lambda = 2\pi/Q_1 \qquad (4)$$

The FSDP for glassy $M(eba)_3[M'Cl_4]$ is at $0.9-1.0$ Å^{-1}, which corresponds to a density modulation wavelength of $6.3-7$ Å that is consistent with density modulation characteristic of the crystalline network. This suggests that a network structure reminiscent of the parent crystalline phase is maintained within the glass. Interestingly, a larger amplitude of the oscillatory signal that extends to higher r is observed for $Mn(eba)_3[ZnCl_4]$ relative to $Mn(eba)_3[MnCl_4]$ and **1**-Mn/Co(Zn) (Figure 5a, inset; Figure S25). This implies that a higher degree of extended structural ordering is present in $Mn(eba)_3[ZnCl_4]$, which could contribute to its faster crystallization kinetics.

While peaks at short interatomic distances remain largely unchanged upon heating each glass, changes to intermediate and long-range PDF features provide insight into structural evolution across the glass–crystal transitions. Arising from metal–metal correlations in the intermediate range, broad peaks centered at 7.8 and 14.5 Å significantly sharpen and increase in intensity as metal–metal distances unify during crystallization (Figure 5b). To quantitatively analyze how extended-range density modulations evolve upon heating, the position and width of the FSDP was modeled as a function of temperature for $Mn(eba)_3[MnCl_4]$ and **1**-Mn/Co(Zn) (Figures S26 and S27). As crystallization occurs in both compounds, the FSDP decreases in width and increases in intensity, consistent with increased structural order.

The position of the FSDP is 0.91 Å^{-1} in the glass state of $Mn(eba)_3[MnCl_4]$, while the first intense Bragg peak appears at a higher Q of 0.95 Å^{-1} in the crystalline state, which suggests a contraction in real-space density modulations during crystallization. Surprisingly, He pycnometry shows that the density of the $Mn(eba)_3[MnCl_4]$ glass is actually 3.0% higher than that of the crystal (Figure S42). We hypothesize that the slight increase in the glassy state density is mainly driven by a reduction in tiny void spaces between ordered layers in the glass relative to the crystalline state, which is not captured in the FSDP since it only reports on weakly ordered density modulations. This is consistent with the dynamic disorder observed for $[M'Cl_4]^{2-}$ anions (Figure S4), which could reflect voids in between the coordination network layers that are eliminated in the glassy state and regained upon the glass–crystal transition. Although not commonly observed for conventional glasses, we note that there are several examples of metal–organic frameworks that form glasses that are denser than the parent crystalline phase due to reduced residual void space.[15b]

Optical Contrast across Reversible Glass–Crystal Transitions. For rewriteable data storage and phase-change memory applications, changes in optical properties between the crystal and glass phases of a material can be used to read out a current logic state (0 or 1). Given the fine control over melting, glass, and cold crystallization transitions that can be achieved, we anticipated that $M(eba)_3[M'Cl_4]$ compounds containing optically active metal centers within the coordination network would serve as promising optical phase-change materials owing to changes in the absorption intensity of $d-d$ transitions as centrosymmetric, six-coordinate metal centers in

the crystalline network transition to non-centrosymmetric, lower-coordinate species in the glassy network. To begin investigating this, we fabricated smooth, homogeneous films (thickness of 10 ± 5 μm) of single and binary $M(eba)_3[M'Cl_4]$ glasses via melt quenching that could be converted into crystalline films by annealing at T_x (Figure S32). While no visible color change is observed for $Mn(eba)_3[ZnCl_4]$ and the purple to dark blue color change of $Co(eba)_3[CoCl_4]$ is irreversible, the binary glass **1**-Mn/Co(Zn) excitingly combines the high reversibility and substantial optical contrast of the two parent phases. Specifically, the glass–crystal transition for **1**-Mn/Co(Zn) occurs with a distinct, reversible color change from dark blue to a faint pale blue (Figure 7b, inset).

To confirm the molecular mechanism responsible for the color change, we collected ambient-temperature UV–vis spectra for both glassy and annealed crystalline films of **1**-Mn/Co(Zn) sandwiched between two pieces of optically transparent quartz slides (Figure 7b, inset). An absorption band at 600–725 nm is present for the annealed crystalline film, along with an additional absorption band of very low intensity centered at 543 nm (Figures 7a and S36). With broad maxima at 612, 629, 665, and 694 nm, the main absorption band in the crystalline state is consistent with $d-d$ transitions for tetrahedral $[CoCl_4]^{2-}$,[37] whereas the significantly weaker absorption band at 543 nm arises from the Laporte-forbidden $d-d$ transitions of octahedral Co coordination centers. While $[CoO_6]^{2+}$ octahedra are expected in the crystalline binary network, the formation of $[CoCl_4]^{2-}$ in the annealed crystal from the initial mixture of $Mn(eba)_3[ZnCl_4]$ and $Co(eba)_3[ZnCl_4]$ suggests some exchange between network Co atoms and Zn atoms of the $[ZnCl_4]^{2-}$ anions during melt quenching and recrystallization. Though quantifying the exact extent of this exchange is challenging, the presence of $[CoCl_4]^{2-}$ in annealed **1**-Mn/Co(Zn) is further confirmed by EXAFS spectra at the Co edge (Figures S20 and S21) as well as by X-ray diffraction data for an analogue of the compound synthesized by a solution-phase crystallization rather than by molten-phase blending (Figure S5 and Table S7). The light blue color of the annealed crystalline film can thus be attributed to a small population of $[CoCl_4]^{2-}$ anions.

Upon melt quenching to form glassy **1**-Mn/Co(Zn), the absorption onset shifts to 500 nm, and there is an increase in absorption intensity, as expected, given the intense blue color of the glass (Figure 7b). Broad features at 609, 626, and 660 nm indicate that $[CoCl_4]^{2-}$ species are still present in the glass. The absorption onset shift and significant enhancement in intensity for glassy **1**-Mn/Co(Zn) compared to crystalline **1**-Mn/Co(Zn) can be attributed primarily to the breaking of inversion symmetry within the coordination network since undercoordinated Co centers ($N_{Co-O} < 6$) have additional allowed $d-d$ transitions. As crystallization occurs, Co centers regain their octahedral coordination environments—with the exception of some residual $[CoCl_4]^{2-}$ anions—and the color reverts from dark blue to pale blue. Importantly, the optical switching in this binary glass is highly reversible, with a similar absorbance contrast observed between the glass and crystalline states over the course of at least three thermal cycles (Figure S36).

To more rigorously quantify the absorbance contrast, we determined the absorption coefficients of the glass by measuring the absorbance of glass films as a function of thickness (14, 20, 34, 45 μm) (Figure S33). The films were

then annealed to determine the absorption coefficients of the crystalline phase, with diffuse scattering from crystalline domains accounted for by subtracting a fitted baseline over a featureless range ($360 \leq \lambda \leq 440$ nm) of each spectrum. The absorption coefficient at a given wavelength (λ) was then obtained by fitting the dependence of absorbance on estimated thickness with Beer's law:

$$A = \alpha l \qquad (5)$$

where A is the absorbance, α is the absorption coefficient, and l is the estimated film thickness (Figure S35). Notably, **1**-Mn/Co(Zn) features a large $\alpha_{glass}/\alpha_{crystal}$ ratio of 5.4 at 650 nm, which confirms that this material can be converted between two states with high optical contrast (Figure 7b).

To eliminate the effects of diffuse scattering and to allow for a more quantitative comparison to existing chalcogenide glasses that are used in reflection mode for rewritable data storage, we also measured changes in reflectivity across the glass–crystal transition using a spectroscopic microscope (Figure 7c). The high spatial resolution ($\sim$0.3 μm) provided by spectroscopic microscopes—in combination with the large grain size (10–50 μm) of **1**-Mn/Co(Zn) crystals—allowed for the precise quantification of reflectivity from a single crystalline grain. Moreover, a reflective silver backing was used to minimize light loss due to transmission through the sample. Although slightly lower than the theoretical absorptivity ratio of 5.4, a large contrast ratio of 4.8 in percent normalized reflectivity ($\%R_{crystal\_N}/\%R_{glass\_N}$) at 650 nm was observed for the glass–crystal transition of **1**-Mn/Co(Zn) (Figure 7c). The reflectivity values for the glassy and crystalline phases were used to calculate the reflectivity contrast (C), which is a commonly used parameter to evaluate optical contrast in rewriteable optical data storage and is defined as:[38]

$$C = \frac{2(R_{crystal} - R_{glass})}{R_{crystal} + R_{glass}} \times 100\% \qquad (6)$$

where $R_{crystal}$ and R_{glass} correspond to the reflectivity of the crystal and glass phases, respectively. With a C value of 131%, the optical contrast achieved by **1**-Mn/Co(Zn) is higher or comparable to reported chalcogenide phase-change materials.[38,39] In addition, the reflectivity of each phase did not change significantly over multiple melt–recrystallization cycles (Figures 7d and S39). Although the bulk-film sample configuration used here is not conducive to evaluating scaling potential and switching time—which are important parameters for photonic memory applications that require ultrafast switching and small device sizes[23]—**1**-Mn/Co(Zn) demonstrates the potential of utilizing changes in metal–ligand coordination environments across glass–crystal transitions to achieve high optical contrast at significantly lower operating temperatures than chalcogenide phase-change materials, thus providing a pathway to data storage and optical switches with reduced energy intensity.

■ CONCLUSIONS

The foregoing results demonstrate a strategy to increase the glass-transition temperatures of metal–bis(acetamide) networks to above ambient through the use of ethylenebis-(acetamide) as a bridging ligand. The increased T_g—relative to previously reported metal–bis(acetamide) networks—can be attributed to a reduced entropy of fusion and increased molten-phase viscosity that results from the reduced conforma-

tional flexibility of ethylenebis(acetamide) in comparison to longer bridging ligands. Moreover, most $M(eba)_3[M'Cl_4]$ compounds undergo reversible glass–crystal transitions, and the glass stability can be enhanced by modifying the nature of the metal center in the counteranion site or by liquid-phase blending of two $M(eba)_3[M'Cl_4]$ networks. The highly reversible interconversion between glassy and crystalline phases, as well as the capacity for forming homogeneous binary glasses upon liquid-phase mixing, were leveraged to design a new optical phase-change material with a high reflectivity contrast ratio of 4.8. Owing to their high tunability, metal–bis(acetamide) networks offer a promising platform for expanding the structural and chemical diversity of metal–organic glasses with predictable thermophysical properties unobserved in conventional glassy materials.

■ ASSOCIATED CONTENT

ⓈI Supporting Information

The Supporting Information is available free of charge at https://pubs.acs.org/doi/10.1021/jacs.2c10449.

> Additional experimental details, powder X-ray diffraction data, EXAFS data, total X-ray scattering data, pair distribution function analysis, calorimetry data, rheological data analysis, UV–vis data, spectroscopic microscopy data, SEM-EDS analysis, and crystallographic information (PDF)

Accession Codes

■ AUTHOR INFORMATION

Corresponding Author

Jarad A. Mason − *Department of Chemistry & Chemical Biology, Harvard University, Cambridge, Massachusetts 02138, United States;* ⓞ orcid.org/0000-0003-0328-7775; Email: mason@chemistry.harvard.edu

Authors

Mengtan Liu − *Department of Chemistry & Chemical Biology, Harvard University, Cambridge, Massachusetts 02138, United States*

Adam H. Slavney − *Department of Chemistry & Chemical Biology, Harvard University, Cambridge, Massachusetts 02138, United States*

Songsheng Tao − *Department of Applied Physics and Applied Mathematics, Columbia University, New York, New York 10027, United States*

Ryan D. McGillicuddy − *Department of Chemistry & Chemical Biology, Harvard University, Cambridge, Massachusetts 02138, United States*

Cassia C. Lee − *Department of Chemistry & Chemical Biology, Harvard University, Cambridge, Massachusetts 02138, United States*

Malia B. Wenny − *Department of Chemistry & Chemical Biology, Harvard University, Cambridge, Massachusetts 02138, United States;* ⓞ orcid.org/0000-0002-0704-8184

Simon J. L. Billinge − *Department of Applied Physics and Applied Mathematics, Columbia University, New York, New York 10027, United States; Condensed Matter Physics and Materials Science Department, Brookhaven National Laboratory, Upton, New York 11973, United States;* ⓞ orcid.org/0000-0002-9734-4998

Complete contact information is available at:
https://pubs.acs.org/10.1021/jacs.2c10449

Notes

The authors declare no competing financial interest.

■ REFERENCES

(1) (a) Otaigbe, J. U.; Quinn, C. J.; Beall, Q. G. H. Processibility and properties of novel glass-polymer melt blends. *Polym. Compos.* **1998**, *19*, 18−22. (b) Schroers, J. Processing of Bulk Metallic Glass. *Adv. Mater.* **2010**, *22*, 1566−1597. (c) Wisitsorasak, A.; Wolynes, P. G. On the Strength of Glasses. *Proc. Natl. Acad. Sci. U.S.A.* **2012**, *109*, 16068−16072. (d) Ballato, J.; Dragic, P. Glass: The Carrier of Light - a Brief History of Optical Fiber. *Int. J. Appl. Glass Sci.* **2016**, *7*, 413−422.

(2) (a) Angell, C. A. Formation of Glasses from Liquids and Biopolymers. *Science* **1995**, *267*, 1924−1935. (b) Angell, C. A. Liquid Landscape. *Nature* **1998**, *393*, 521−524. (c) Debenedetti, P. G.; Stillinger, F. H. Supercooled Liquids and the Glass Transition. *Nature* **2001**, *410*, 259−267.

(3) Morse, D. L.; Evenson, J. W. Welcome to the Glass Age. *Int. J. Appl. Glass Sci.* **2016**, *7*, 409−412.

(4) Yokoyama, D. Molecular Orientation in Small-Molecule Organic Light-Emitting Diodes. *J. Mater. Chem.* **2011**, *21*, 19187−19202.

(5) Bräuer, G. Large Area Glass Coating. *Surf. Coat. Technol.* **1999**, *112*, 358−365.

(6) *The Use of Glass in Buildings*; Block, V., Ed.; ASTM International: West Conshohocken, PA, 2002.

(7) Deshpande, V. K. Science and Technology of Glassy Solid Electrolytes. *IOP Conf. Ser.: Mater. Sci. Eng.* **2009**, *2*, No. 012011.

(8) Donald, I. W.*Immobilization by Vitrification in Waste Immobilization in Glass and Ceramic Based Hosts: Radioactive, Toxic, and Hazardous Wastes*; Wiley, 2010, pp 121−184.

(9) (a) Ediger, M. D. Perspective: Highly Stable Vapor-Deposited Glasses. *J. Chem. Phys.* **2017**, *147*, 210901−210916. (b) Ediger, M. D.; Gruebele, M.; Lubchenko, V.; Wolynes, P. G. Glass Dynamics Deep in Energy Landscape. *J. Phys. Chem. B* **2021**, *125*, 9052−9068.

(10) (a) Telford, M. The Case for Bulk Metallic Glass. *Mater. Today* **2004**, *7*, 36−43. (b) Greaves, G. N.; Sen, S. Inorganic Glasses, Glass-Forming Liquids and Amorphizing Solids. *Adv. Phys.* **2007**, *56*, 1−166.

(11) (a) Yaghi, O. M.; O'Keeffe, M.; O'Keeffe, M.; Ockwig, N. W.; Ockwing, N. W.; Chae, H. K.; Eddaoudi, M. Reticular Synthesis and the Design of New Materials. *Nature* **2003**, *423*, 705−714. (b) Kitagawa, S.; Kitaura, R.; Noro, S. Functional Porous Coordination Polymers. *Angew. Chem., Int. Ed.* **2004**, *43*, 2334−2375. (c) Yaghi, O. M. Reticular Chemistry: Molecular Precision in Infinite 2D and 3D. *Mol. Front. J.* **2019**, *03*, 66−83.

(12) (a) Ediger, M. D.; Angell, C. A.; Nagel, S. R. Supercooled Liquids and Glasses. *J. Phys. Chem. A* **1996**, *100*, 13200−13212. (b) Ediger, M. D.; Harrowell, P. Perspective: Supercooled Liquids and Glasses. *J. Chem. Phys.* **2012**, *137*, No. 080901.

(13) (a) Bennett, T. D.; Cheetham, A. K. Amorphous Metal−Organic Frameworks. *Acc. Chem. Res.* **2014**, *47*, 1555−1562. (b) Fonseca, J.; Gong, T.; Li, J.; Jiang, H-L. Metal−Organic Frameworks (MOFs) beyond crystallinity: Amorphous MOFs, MOF Liquids and MOF glasses. *J. Mater. Chem. A* **2021**, *9*, 10562−10611.

(14) (a) Bennett, T. D.; Horike, S. Liquid, Glass and Amorphous Solid States of Coordination Polymers and Metal−Organic Frameworks. *Nat. Rev. Mater.* **2018**, *3*, 431−440. (b) Smedskjaer, M. M.; Sorensen, S. S. A glass act. *Nat. Chem.* **2021**, *13*, 723−724. (c) Ma, N.; Horike, S. Metal−Organic Network-Forming Glasses. *Chem. Rev.* **2022**, *122*, 4163−4203.

(15) (a) Bennett, T. D.; Tan, J-C.; Yue, Y.; Baxter, E.; Ducati, C.; Terrill, N. J.; Yeung, H. H. -M.; Zhou, Z.; Chen, W.; Henke, S.; Cheetham, A. K.; Greaves, G. N. Hybrid Glasses from Strong and Fragile Metal−Organic Framework liquids. *Nat. Commun.* **2015**, *6*, No. 8079. (b) Bennett, T. D.; Yue, Y.; Li, P.; Qiao, A.; Tao, H.; Greaves, N. G.; Richards, T.; Lampronti, G. I.; Redfern, S. A. T.; Blanc, F.; Farha, O. K.; Hupp, J. T.; Cheetham, A. K.; Keen, D. A. Melt-Quenched Glasses of Metal−Organic Frameworks. *J. Am. Chem. Soc.* **2016**, *138*, 3484−3492. (c) Gaillac, R.; Pullumbi, P.; Beyer, K. A.; Chapman, K. W.; Keen, D. A.; Bennett, T. D.; Coudert, F. X. Liquid Metal−Organic Frameworks. *Nat. Mater.* **2017**, *16*, 1149−1154.

(16) (a) Umeyama, D.; Horike, S.; Inukai, M.; Itakura, T.; Kitagawa, S. Reversible Solid-to-Liquid Phase Transition of Coordination Polymer Crystals. *J. Am. Chem. Soc.* **2015**, *137*, 864−870. (b) Nagarkar, S. S.; Kurasho, H.; Duong, N. T.; Nishiyama, Y.; Kitagawa, S.; Horike, S. Crystal Melting and Glass Formation in Copper Thiocyanate Based Coordination Polymers. *Chem. Commun.* **2019**, *55*, 5455−5458.

(17) (a) Shaw, B. K.; Hughes, A. R.; Maxime, D.; Moss, S.; Anup, D.; Sapnik, A. F.; Thorne, M. F.; McHugh, L. N.; Pugliese, A.; Keeble, D. S.; Chater, P.; Bermudez-Garcia, J. M.; Xavier, M.; Saha, S. K.; Keen, D. A.; Courdert, F.-X.; Blanc, F.; Bennett, T. D. Melting of Hybrid organic−inorganic perovskites. *Nat. Chem.* **2021**, *13*, 778−785. (b) Singh, A.; Jana, M. K.; Mitzi, D. B. Reversible Crystal−Glass Transition in a Metal Halide Perovskite. *Adv. Mater.* **2021**, *33*, No. 2005868. (c) Shaw, B. K.; Castillo-Blas, C.; Thorne, M. F.; Gómez, M. L. R.; Forrest, T.; Lopez, M. D.; Chater, P. A.; McHugh, L. N.; Keen, D. A.; Bennett, T. D. Principles of Melting in Hybrid Organic−Inorganic Perovskite and Polymorphic ABX$_3$ Structures. *Chem. Sci.* **2022**, *13*, 2033−2042.

(18) Stillinger, F. H. A Topographic View of Supercooled Liquids and Glass Formation. *Science* **1995**, *267*, 1935−1939.

(19) Liu, M.; McGillicuddy, R. D.; Vuong, H.; Tao, S.; Slavney, A. H.; Gonzalez, M. I.; Billinge, S. J. L.; Mason, J. A. Network-Forming Liquids from Metal−Bis(acetamide) Frameworks with Low Melting Temperatures. *J. Am. Chem. Soc.* **2021**, *143*, 2801−2811.

(20) (a) Ishihara, T.; Arimoto, S.; Kumable, H.; Murotani, T. Zone-melting recrystallization of silicon thin films for solar cell application. *Prog. Photovoltaics* **1995**, *3*, 105−113. (b) Zheng, Y.; Zhang, J.; Sun, X.; Li, H.; Ren, Z.; Yan, S. Crystal Structure Regulation of Ferroelectric Poly(vinylidenefluoride) via Controlled Melt−Recrystallization. *Ind. Eng. Chem. Res.* **2017**, *56*, 4580−4587.

(21) (a) Beall, G. H. Design and Properties of Glass-Ceramics. *Annu. Rev. Mater. Sci.* **1992**, *22*, 91−119. (b) Rüssel, C. Oriented Crystallization of Glass. A Review. *J. Non-Cryst. Solids.* **1997**, *219*, 212−218.

(22) (a) Wong, H.-S. P.; Raoux, S.; Kim, S.; Liang, J.; Reinfenberg, J. P.; Ragendran, B.; Asheghi, M.; Goodson, K. E. Phase Change Memory. *Proc. IEEE* **2010**, *98*, 2201−2227. (b) Raoux, S.; Xiong, F.; Wuttig, M.; Pop, E. Phase Change Materials and Phase Change Memory. *MRS Bull.* **2014**, *39*, 703−710.

(23) (a) Wuttig, M.; Bhaskaran, H.; Taubner, T. Phase-Change Materials for Non-volatile Photonic Applications. *Nat. Photonics* **2017**, *11*, 465−476. (b) Wei, Z.; Riccardo, M.; Matthias, W.; Evan, M. Designing Crystallization in Phase-Change Materials for Universal Memory and Neuro-Inspired Computing. *Nat. Rev. Mater.* **2019**, *4*, 150−168. (c) Zhang, Y.; Ríos, C.; Shalaginov, M. Y.; Li, M.; Majumdar, A.; Gu, T.; Hu, J. Myths and Truths about Optical Phase Change Materials: A Perspective. *Appl. Phys. Lett.* **2021**, *118*, No. 210501.

(24) (a) Lankhorst, M. H. R. Modelling Glass Transition Temperatures of Chalcogenide Glasses. Applied to Phase-Change Optical Recording Materials. *Journal of Non-Crystalline Solids* **2002**, *297*, 210−219. (b) Raoux, S.; Welnic, W.; Ielmini, D. Phase Change Materials and Their Application to Nonvolatile Memories. *Chem. Rev.* **2010**, *110*, 240−267.

(25) (a) Okabe, K. L.; Sood, A.; Yalon, E.; Neumann, C. M.; Asheghi, M.; Pop, E.; Goodson, K. E.; Wong, H.-S. P. Understanding the Switching Mechanism of Interfacial Phase Change Memory. *J. Appl. Phys.* **2019**, *125*, No. 184501. (b) Stern, K.; Wainstein, N.; Keller, Y.; Neumann, C. M.; Pop, E.; Kvatinsky, S.; Yalon, E. Uncovering Phase Change Memory Energy Limits by Sub-Nano-second Probing of Power Dissipation. *Adv. Electron. Mater.* **2021**, *7*, No. 21000217.

(26) Horike, S.; Nagarkar, S. S.; Ogawa, T.; Kitagawa, S. A New Dimension for Coordination Polymers and Metal−Organic Frameworks: Towards Functional Glasses and Liquids. *Angew. Chem., Int. Ed.* **2020**, *59*, 6652−6664.

(27) Dannenfelser, R-M.; Yalkowsky, S. H. Estimation of Entropy of Melting from Molecular Structure: A Non-Group Contribution Method. *Ind. Eng. Chem. Res.* **1996**, *35*, 1483−1486.

(28) Zheng, Q.; Zhang, Y.; Montazerian, M.; Gulbiten, O.; Mauro, J. C.; Zanotto, E. D.; Yue, Y. Understanding Glass through Differential Scanning Calorimetry. *Chem. Rev.* **2019**, *119*, 7848−7939.

(29) Hrubý, A. Evaluation of glass-forming tendency by means of DTA. *Czech. J. Phys. B* **1972**, *22*, 1187−1193.

(30) Avrami, M. Kinetics of Phase Change. II Transformation-Time Relations for Random Distribution of Nuclei. *J. Chem. Phys.* **1940**, *8*, 212−224.

(31) Marques, L. E.; Costa, A. M. C.; Crovace, M. C.; Rodrigues, A. C. M.; Cabral, A. A. Influence of Particle Size on Nonisothermal Crystallization in a Lithium Disilicate Glass. *J. Am. Ceram. Soc.* **2015**, *98*, 774−780.

(32) Longley, L.; Collins, S. M.; Zhou, C.; Smales, G. J.; Norman, S. E.; Brownbill, N. J.; Ashling, C. W.; Chater, P. A.; Tovey, R.; Schönlieb, C.-B.; Headen, T. F.; Terrill, N. J.; Yue, Y.; Smith, A. J.; Blanc, F.; Keen, A. D.; Midgley, P. A.; Bennett, T. D. Liquid Phase Blending of Metal−Organic Frameworks. *Nat. Commun.* **2018**, *9*, No. 2135.

(33) (a) Egami, T.; Billinge, S. J. L.*Underneath the Bragg Peaks: Structural Analysis of Complex Materials*, 2nd ed.; Elsevier: Amsterdam, 2012. (b) Juhás, P.; Davis, T.; Farrow, C. L.; Billinge, S. J. L. PDFgetX3: A Rapid and Highly Automatable Program for Processing Powder Diffraction Data into Total Scattering Pair Distribution Functions. *J. Appl. Crystallogr.* **2013**, *46*, 560−566.

(34) (a) Thorpe, M. F.*Rigidity Percolation*. In *Physics of Disordered Materials*; Alder, D.; Fritzsche, H.; Ovshinsky, S. R., Eds.; Springer: Boston, 1985; pp 55−61. (b) Phillips, J. C.; Thorpe, M. F. Constraint Theory, Vector Percolation and Glass Formation. *Solid. State Commun.* **1985**, *53*, 699−702.

(35) (a) Salmon, P. S. Real Space Manifestation of the First Sharp Diffraction Peak in the Structure Factors of Liquid and Glassy Materials. *Proc. R. Soc. London, Ser. A* **1992**, *A437*, 351−365. (b) Doan-Nguyen, V. V. T.; Kimber, S. A. J.; Pontoni, D.; Reifsnyder Hickey, D.; Diroll, B. T.; Yang, X.; Miglierini, M.; Murray, C. B.; Billinge, S. J. L. Bulk Metallic Glass-like Scattering Signal in Small Metallic Nanoparticles. *ACS Nano* **2014**, *8*, 6163−6170.

(36) (a) Moss, S. C.; Price, D. L.*Physics of Disordered Materials*; Adler, A.; Fritzsche, H.; Ovshinsky, S. R., Eds.; Plenum: New York, 1985; p 77. (b) Elliott, S. Extended-range Order, Interstitial Voids, and the First Sharp Diffraction Peak of Network Glasses. *J. Non-Cryst. Solids* **1995**, *182*, 40−48.

(37) (a) Banić, N.; Vraneš, M.; Abramović, B.; Csanádia, J.; Gadžurić, S. Thermochromism, Stability and Thermodynamics of Cobalt(II) Complexes in Newly Synthesized Nitrate Based Ionic Liquid and Its Photostability. *Dalton Trans.* **2014**, *43*, 15515−15525. (b) Uchikoshi, M. Determination of the Distribution of Cobalt-Chloro Complexes in Hydrochloric Acid Solutions at 298 K. *J. Solution Chem.* **2018**, *47*, 2021−2038.

(38) Liu, F.; Liu, C.; Men, L.; Liu, H. In *Dynamic Properties of GeSbTe-Based Optical Disk at 680 nm*, Proc. SPIE 2931 of the Fourth International Symposium on Optical Storage; SPIE: Shenzhen, China, April 22-26, 1996; pp 13−18.

(39) (a) Medower, B. S.; Redmond, I. R.; Davies, D. H.*Optical Data Storage Media with Enhanced Contrast*. US73682222008. (b) Yama-da, N.; Kojima, R.; Nishihara, T.; Tsuchino, A.; Tomekawa, Y.; Kusada, H. In *100 GB Rewritable Triple-layer Optical Disk Having Ge-Sb-Te Films*, Proceedings of the European Phase Change and Ovonic Science Symposium; Aachen, Germany, 2009; pp 23−28.